

# Journal of Geophysical Research: Solid Earth

## RESEARCH ARTICLE

10.1002/2015JB012483

**Key Points:**

- We analyze shear wave splitting in the SJFZ using a new data set including five linear arrays
- We find clear contrast of fast directions between the SW and NE sides of the SJFZ
- Fast directions vary significantly on across-fault arrays with station spacing at tens of meters

**Supporting Information:**

- Figures S1–S6 and Tables S1 and S2

**Correspondence to:**

Z. Li,  
zli354@gatech.edu

**Citation:**

Li, Z., Z. Peng, Y. Ben-Zion, and F. L. Vernon (2015), Spatial variations of shear wave anisotropy near the San Jacinto Fault Zone in Southern California, *J. Geophys. Res. Solid Earth*, 120, 8334–8347, doi:10.1002/2015JB012483.

Received 29 AUG 2015

Accepted 27 OCT 2015

Accepted article online 31 OCT 2015

Published online 2 DEC 2015

## Spatial variations of shear wave anisotropy near the San Jacinto Fault Zone in Southern California

**Zefeng Li<sup>1</sup>, Zhigang Peng<sup>1</sup>, Yehuda Ben-Zion<sup>2</sup>, and Frank L. Vernon<sup>3</sup>**

<sup>1</sup>School of Earth and Atmospheric Sciences, Georgia Institute of Technology, Atlanta, Georgia, USA, <sup>2</sup>Department of Earth Sciences, University of Southern California, Los Angeles, California, USA, <sup>3</sup>Scripps Institution of Oceanography, University of California, San Diego, La Jolla, California, USA

**Abstract** We examine crustal anisotropy at several scales along and across the San Jacinto Fault Zone (SJFZ) by systematically measuring shear wave splitting (SWS) parameters. The analyzed data are recorded by 86 stations during 2012–2014, including five linear dense arrays crossing the SJFZ at different locations and other autonomous stations within 15 km from the main fault trace. Shear phase arrivals and SWS parameters (fast directions and delay times) are obtained with automated methods. The measurement quality is then assessed using multiple criteria, resulting in 23,000 high-quality measurements. We find clear contrast of fast directions between the SW and NE sides of the SJFZ. Stations on the SW side have fast directions consistent overall with the maximum horizontal compression direction (SHmax), while stations on the NE side show mixed patterns likely reflecting lithological/topographic variations combined with fault zone damage. The fast directions in the Anza gap section with relatively simple fault geometry agree with the inferred SHmax, and the delay times at an array within that section are smaller than those observed at other across-fault arrays. These indications of less pronounced damage zone in the Anza section compared to other segments of the SJFZ are correlated generally with geometrical properties of the surface traces. Significant variations of fast directions on several across-fault arrays, with station spacing on the orders of a few tens of meters, suggest that shallow fault structures and near-surface layers play an important role in controlling the SWS parameters.

### 1. Introduction

Shear wave splitting (SWS) refers to a phenomenon that seismic shear waves propagating through an anisotropic medium split into two orthogonally polarized waves with different velocities. The interior of the earth is anisotropic to different levels at different depth sections owing to many factors. Crustal anisotropy may be considered as a result of preferential alignment of fluid-filled cracks that are parallel to the direction of maximum horizontal compressive stress SHmax [Nur and Simmons, 1969; Crampin et al., 1978; Leary et al., 1990]. However, studies associated with large strike-slip faults usually observe fast directions that are parallel to the fault strike, especially for stations close to the fault trace [e.g., Peng and Ben-Zion, 2004; Boness and Zoback, 2006; Audet, 2014; Rasendra et al., 2014], consistent with elevated rock cracking along the fault zones [e.g., Finzi et al., 2009; Hamiel et al., 2009]. Other causes of crustal anisotropy include preferential mineral alignment, remnant features of paleostress, and sedimentary layering [Alford, 1986; Sayers, 1994; Aster and Shearer, 1992]. In general, a mixture of mechanisms on a single station can be produced due to different raypaths of seismic events [e.g., Cochran et al., 2003; Peng and Ben-Zion, 2004].

Analysis of SWS has been extensively conducted along a number of major fault zones. Examples include the San Andreas Fault [Silver and Savage, 1994; Boness and Zoback, 2006; Liu et al., 2008], the San Jacinto Fault [e.g., Peacock et al., 1988; Crampin et al., 1990; Aster et al., 1990; Yang et al., 2011], the North Anatolian fault [e.g., Peng and Ben-Zion, 2004; Eken et al., 2013], the Chelongpu fault [Liu et al., 2004], the Nojima fault [Tadokoro and Ando, 2002], and the Marlborough fault [Balfour et al., 2005]. These studies primarily focused on spatial distributions of shear wave anisotropy, providing important constraints on their physical mechanisms and spatial extent of the fault damage zone [Li et al., 1994; Shih and Meyer, 1990; Zhang and Schwartz, 1994; Peng and Ben-Zion, 2004; Li et al., 2014]. Temporal variations of SWS parameters associated with earthquake occurrence and volcano eruptions have been reported, sometimes with controversy [e.g., Crampin et al., 1990; Aster et al., 1990; Tadokoro and Ando, 2002; Gerst and Savage, 2004; Crampin and Gao, 2004; Liu et al., 2005; Peng and Ben-Zion, 2005; Uglert et al., 2011; Godfrey et al., 2014].

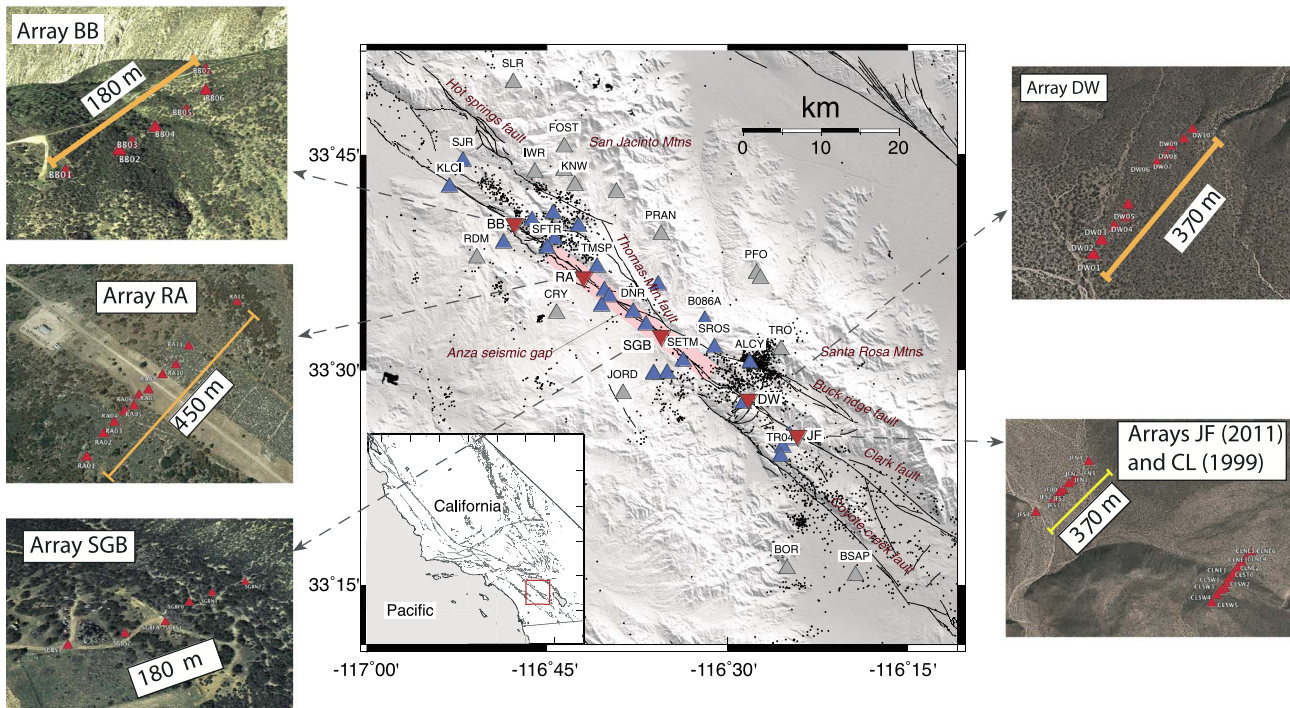


**Figure 1.** Map showing the study region along the San Jacinto Fault in Southern California. Active faults in this region are marked as black lines, and seismicity ( $1 < M < 4$ ) between 1 January 2012 and 6 February 2014 is marked as black dots. Blue and gray triangles are individual stations within and outside 5 km from the main fault trace. Inverted triangles are across-fault arrays whose zoom-in plots are shown on top of Google map. The inset shows a map of California with the red rectangle marking the location of the study region.

High-resolution spatial variations of anisotropy around active faults can be achieved with data of dense arrays close to the fault. For example, Cochran *et al.* [2003, 2006] used dense cross-fault arrays to study spatiotemporal variations anisotropy following the 1999  $M_{\text{W}} 7.1$  Hector Mine and the 2004  $M_{\text{W}} 6.0$  Parkfield earthquakes. Such closely spaced stations provide more reliable and detailed measurements of near-fault anisotropy parameters at resolutions on the order of tens of meters.

The San Jacinto Fault Zone (SJFZ) is an important target for SWS analysis, due to its structural complexity, highly active seismicity, and dense seismic instrumentation. The SJFZ contains multiple fault segments that have different slip rates and seismic behaviors [e.g., Fialko, 2006; Sanders and Kanamori, 1984]. Since 1890, a number of moderate earthquakes ( $M > 6$ ) have occurred along portions of the SJFZ [Sykes and Nishenko, 1984; Sanders and Kanamori, 1984]. The Anza seismic gap has not experienced any major earthquakes in the past 200 years [Salisbury *et al.*, 2012], although paleoseismic investigations suggest over 20 large earthquakes in the past 4000 years in the region [Rockwell *et al.*, 2015].

In the present paper we conduct a comparative study of within-, near-, and off-fault crustal anisotropy, using local earthquake data from January 2012 to June 2014 recorded by five spatially dense linear arrays that cross the SJFZ at several locations and other temporary and permanent near-fault stations (Figure 1). Although several SWS studies using local seismic data have been conducted in this region [e.g., Peacock *et al.*, 1988; Aster and Shearer, 1992; Yang *et al.*, 2011], our study utilizes new data sets with dense cross-fault arrays and provides detailed results on spatial variations of near-fault anisotropy. We obtain SWS measurements using an automatic MFAST code [Savage *et al.*, 2010] and compare fast directions with SHmax to identify various features along and across the SJFZ. The results show clear contrast of fast directions between the SW and NE sides of the fault and among different fault zone sections. In the localized Anza seismic gap area, low delay times and fast directions that are quasi-parallel to SHmax are observed. In the other more complex sections of the SJFZ diverse patterns are found. Notable variations of fast directions along several cross-fault arrays document significant changes of fault zone shear anisotropy at scales of tens of meters.

## 2. Data

To investigate fault mechanics and evolutionary behavior of the SJFZ, data were used from a dense seismic network (Figure 1) deployed around the SJFZ between 2010 and 2014 [e.g., Allam *et al.*, 2014; Kurzon *et al.*, 2014]. The deployment includes five small-aperture linear arrays with instrument spacing 25–50 m across several segments of the SJFZ and additional near-fault stations. From NW to SE, the five linear arrays are Black Burn (BB), Ramona (RA), Sage Brush (SB), Dry Wash (DW), and Jackass Flat (JF). The linear arrays were deployed approximately perpendicular to the surface trace of the fault, with lengths ranging from ~180 m to ~450 m. To compare on- and off-fault anisotropy and augment the along-strike measurements, we also include 42 temporary and permanent stations within 15 km from the main SJFZ trace, which is approximated by a line passing through the center of the SGB array (33.5397°N, 116.5917°W) with an azimuth of 127° (Figure 1).

The analyzed data consist of local earthquakes listed in the Southern California Seismic Network catalog from January 2012 to June 2014, during which the linear arrays were operational. We select events using the following criteria: (1) magnitude larger than 1 but less than 4 to ensure signal-noise-ratio and avoid strong source effects, (2) close to the examined station, i.e., epicentral distance less than 25 km from the station or array center, and (3) incident angle < 45° assuming a straight raypath (i.e., depth larger than the epicentral distance) to avoid interference of converted phases [Booth and Crampin, 1985]. These criteria result in data associated with 2697 local earthquakes and 22,548 waveforms recorded by the five linear arrays and 22,033 waveforms recorded by other on- and off-fault stations. On average each station recorded data associated with a few hundred up to 1000 events (Tables S1 and S2 in the supporting information).

## 3. Method

Because the analyzed data set is relatively large, it is more efficient (and objective) to pick *S* phases automatically. We use a “predict-and-search” method for automatic picking of *S* phases [Li and Peng, 2015]. The method has the following steps: (1) compute theoretical arrival using a reference velocity model; (2) search for arrival around the expected theoretical time using a signal-to-noise ratio function; (3) with these candidate picks, invert for improved velocity model starting with the initial reference model; and (4) repeat steps 1–3 until picks and velocity models become stable. We start with a 1-D velocity model of 5 km spacing in depth and velocity value averaged from the Southern California Earthquake Center community 3-D velocity model [Magistrale *et al.*, 1996]. The *S* phases are picked on horizontal components, and only those with signal-to-noise ratio (SNR) > 3 are used. To ensure the consistency of *S* picks among the stations in each linear array, we align the *S* picks on the stations in each array with waveform cross correlations (Figure 2). For other fault zone stations, we simply use the picks from the predict-and-search method. We note that small pick inaccuracy is unlikely to affect the SWS measurement significantly. The SWS measuring algorithm, outlined below, analyzes multiple time windows around the pick and uses the best results. The algorithm’s flexibility in the precise choice of time window start and end makes it insensitive to small changes in pick arrivals of tenths of seconds.

Fast directions and delay times are computed using the automated program MFAST [Savage *et al.*, 2010]. The code determines the splitting parameters using the covariance matrix method of Silver and Chan [1991]. It performs grid search over the fast direction-delay time ( $\Phi$ - $\delta t$ ) space to minimize the energy on the component perpendicular to the initial polarization of shear waves. This process is applied over multiple measurement windows. The minimum and maximum window lengths are set using the dominant period of each waveform. Cluster analysis is then performed to determine the best solution among all the windows [Teanby *et al.*, 2004]. The code also uses an automatic algorithm to determine the best band-pass filter for single measurement in terms of the tradeoff between frequency bandwidth and SNR. However, because the dominant frequency for shear waves of local earthquakes is 5–10 Hz, we fix the band-pass filter to be 1–15 Hz and apply this to all the data [Yang *et al.*, 2011]. Figure 3 illustrates the analysis procedure with data of one example event.

The MFAST program also provides multiple parameters for assessing the measurement quality. Here we select measurements that satisfy: (1) SNR > 3; (2) delay time  $\delta t$  < 0.4 s and  $\delta t$  error < 0.1 s; (3) fast direction  $\Phi$  error < 15°; (4) cluster grade A and B (referring to Savage *et al.* [2010] for definition); and (5) 20° < polarization angle of fast wave against incoming wave < 70° [Peng and Ben-Zion, 2004]. These criteria are either empirical or inherent from previous studies [e.g., Peng and Ben-Zion, 2004; Savage *et al.*, 2010]. Out of 44,300 event-station pairs, 23,000 high-quality measurements (~52%) are obtained and used in subsequent studies.

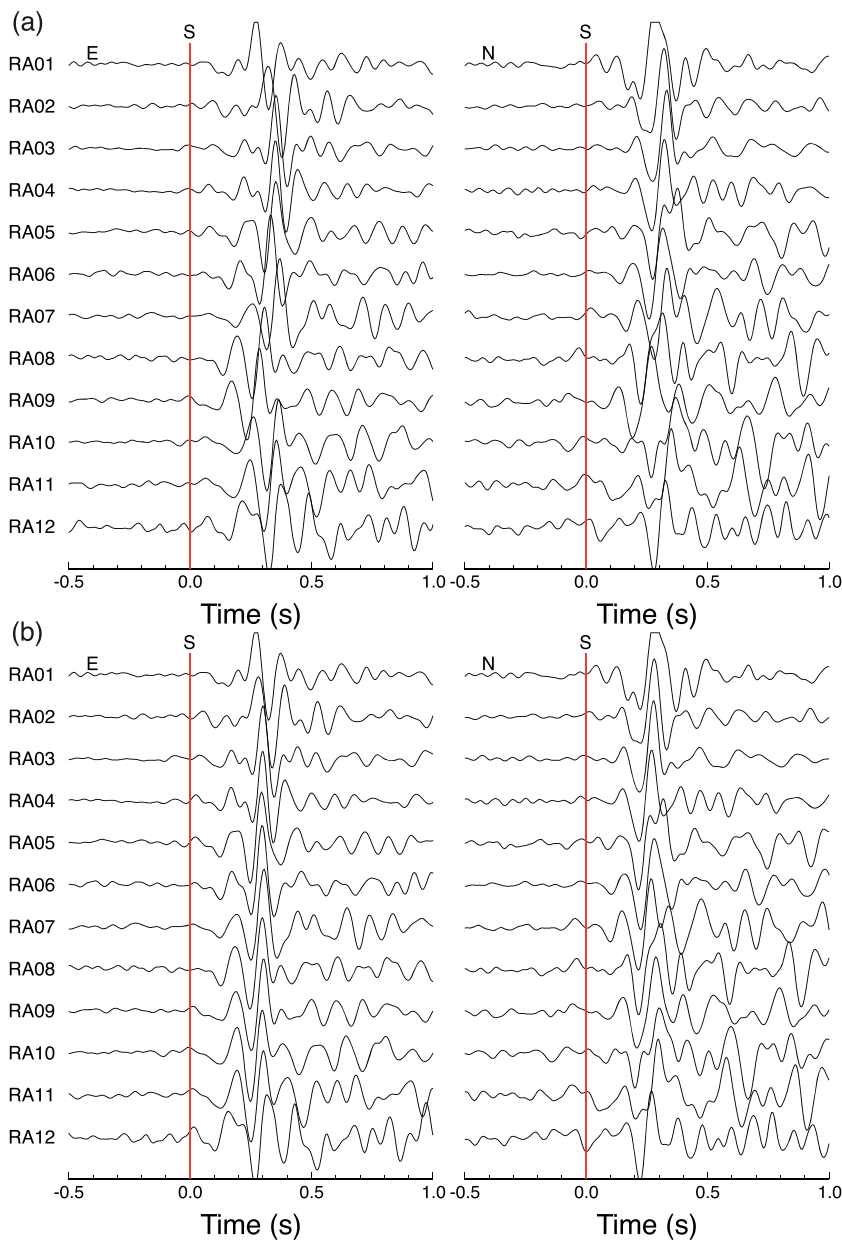


**Figure 2.** An example of automatically picked  $S$  arrivals on RA array. (a) Automatic  $S$  picks on  $E$  and  $N$  components using the predict-and-search method [Li and Peng, 2015]. (b)  $S$  picks that are refined by waveform cross correlation on basis of Figure 2a.

The statistical analysis of  $\Phi$  is performed generally using the von Mises method [e.g., Mardia and Jupp, 2000; Cochran et al., 2003; Peng and Ben-Zion, 2004; Yang et al., 2011]. This method essentially treats fast directions as vectors with unit length and averages them as a mean. However, there is a drawback when the fast direction distribution is bimodal or scattered. For example, if a station has two groups of preferential directions at  $0^\circ$  and  $90^\circ$  controlled by different mechanisms, the mean value from von Mises method would be  $45^\circ$ , with no physical meaning. Therefore, we only use the resultant length  $R$  (ranging from 0 to 1) to quantify the variance of the directions. For the dominant directions, we use a  $10^\circ$  long sliding window to calculate the number of measurements within that window and shift the window every  $1^\circ$  between  $0^\circ$  and  $180^\circ$ . Given the  $180^\circ$  ambiguity of fast direction, special treatment is needed near the boundaries. For example, the number of measurements within the window centered at angle  $0^\circ$  is counted in the range of  $(0^\circ\text{--}5^\circ)$  and  $(175^\circ\text{--}180^\circ)$ . Finally, the center of the window with most measurements is taken as the dominant fast direction.

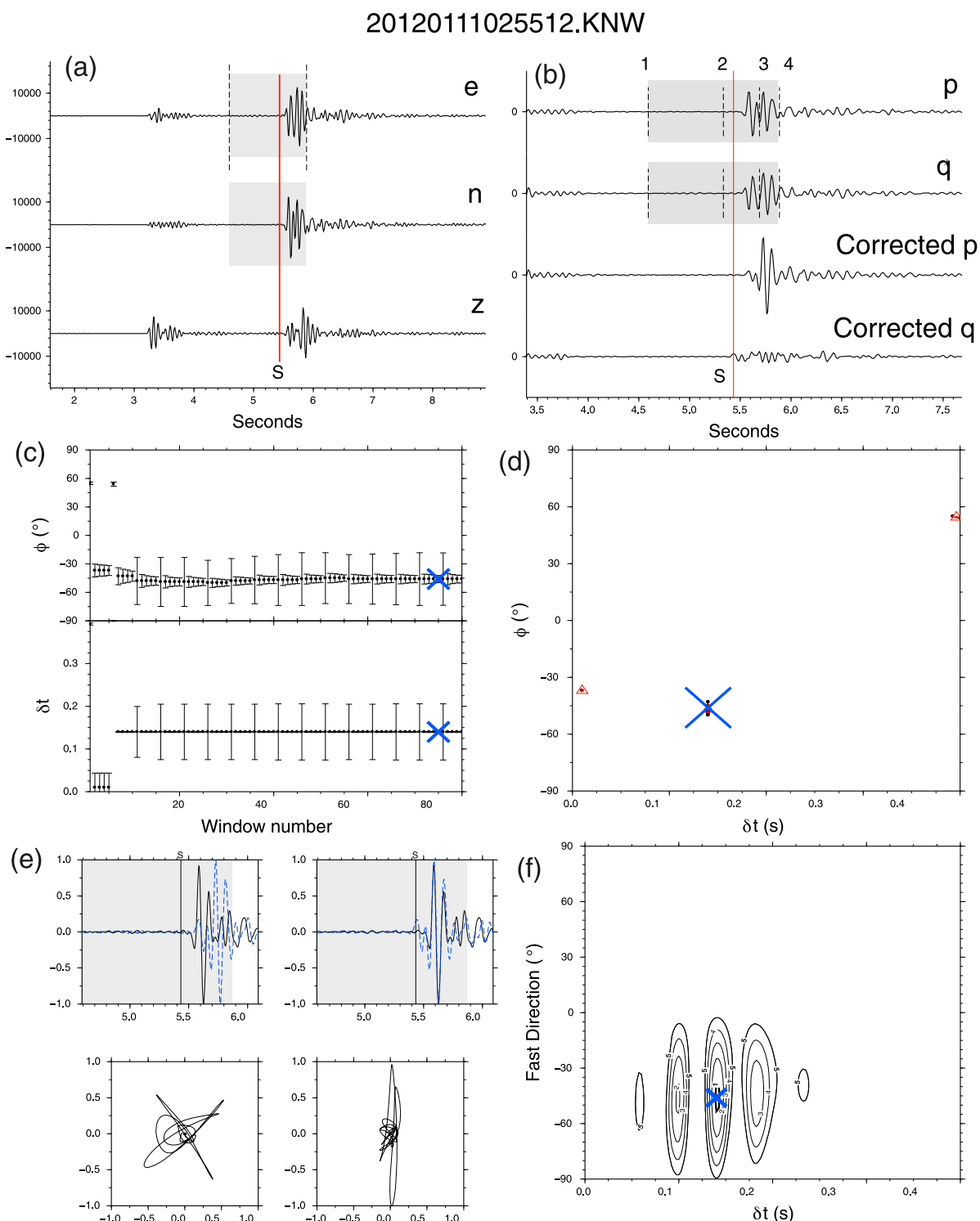


**Figure 3.** An example of automatic SWS analysis on an M1.13 event (event ID 15235601) recorded at station KNW. (a) 1–15 Hz filtered waveform. Red line marks the S pick. The vertical dashed lines and the gray shading mark the time window used in the SWS analysis. (b) The top two components that are rotated to incoming polarization parallel (p) and perpendicular (q) directions. The bottom two are components corrected with the determined delay time and fast direction. Dash lines mark the possible range for the starting (1 and 2) and ending (3 and 4) of the window. (c) The fast directions and delay times that are determined from 80 different time windows. (d) The distributions of fast directions and delay times determined from different time windows. The blue cross marks the best cluster based on the criteria outlined in Teaney et al. [2004]. (e) Waveforms (top row) and particle motions (bottom row) for the original (left column) and SWS corrected (right column) waveforms. (f) Contours of the second eigenvalue of the covariance matrix for difference fast directions and delay times. The blue cross corresponds to the best fitting parameters (delay time  $\delta t = 0.15$  s, fast direction  $\Phi = -45^\circ$ ).

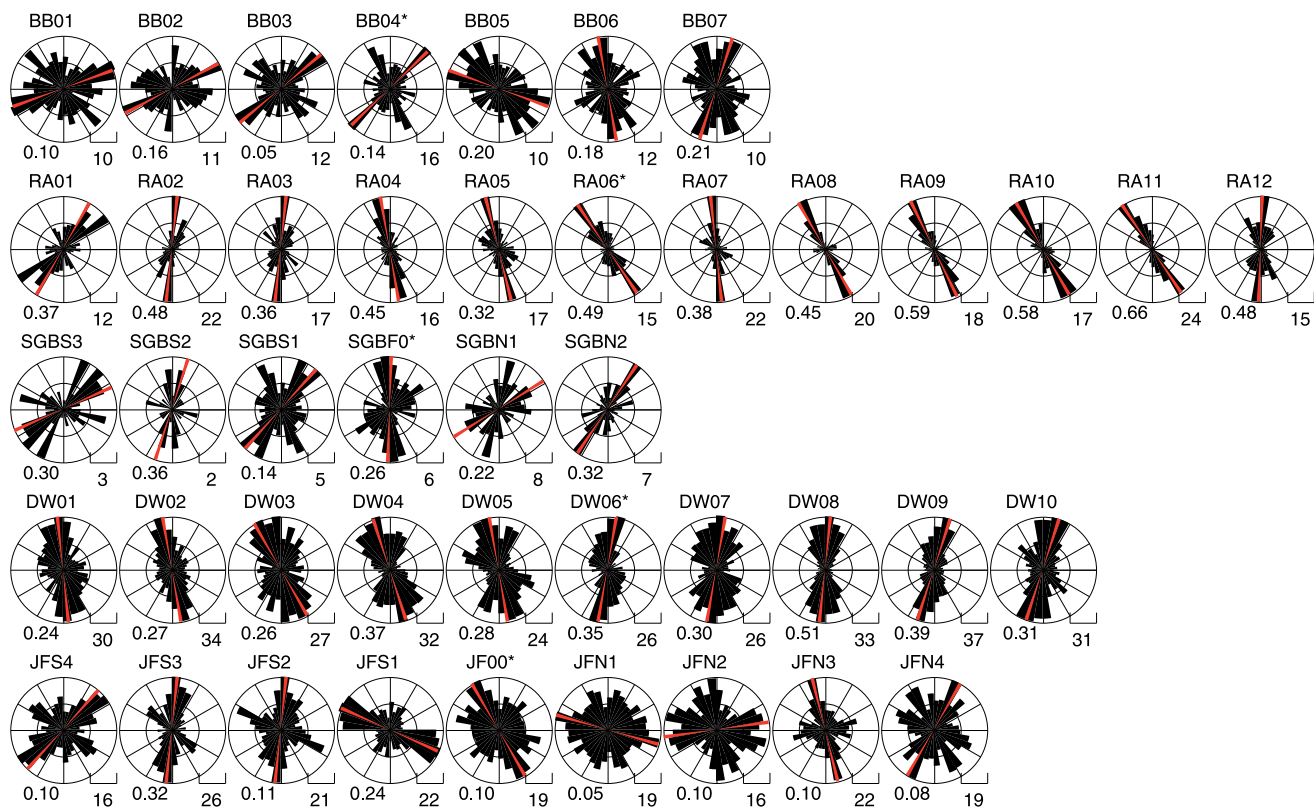


**Figure 4.** Rose diagrams of the fast directions on the five cross-fault arrays. The number at the lower right denotes the number of measurement for unit length. The number at the lower left denotes the resultant length. For each array the station from left to right corresponds to SW to NE across the fault.

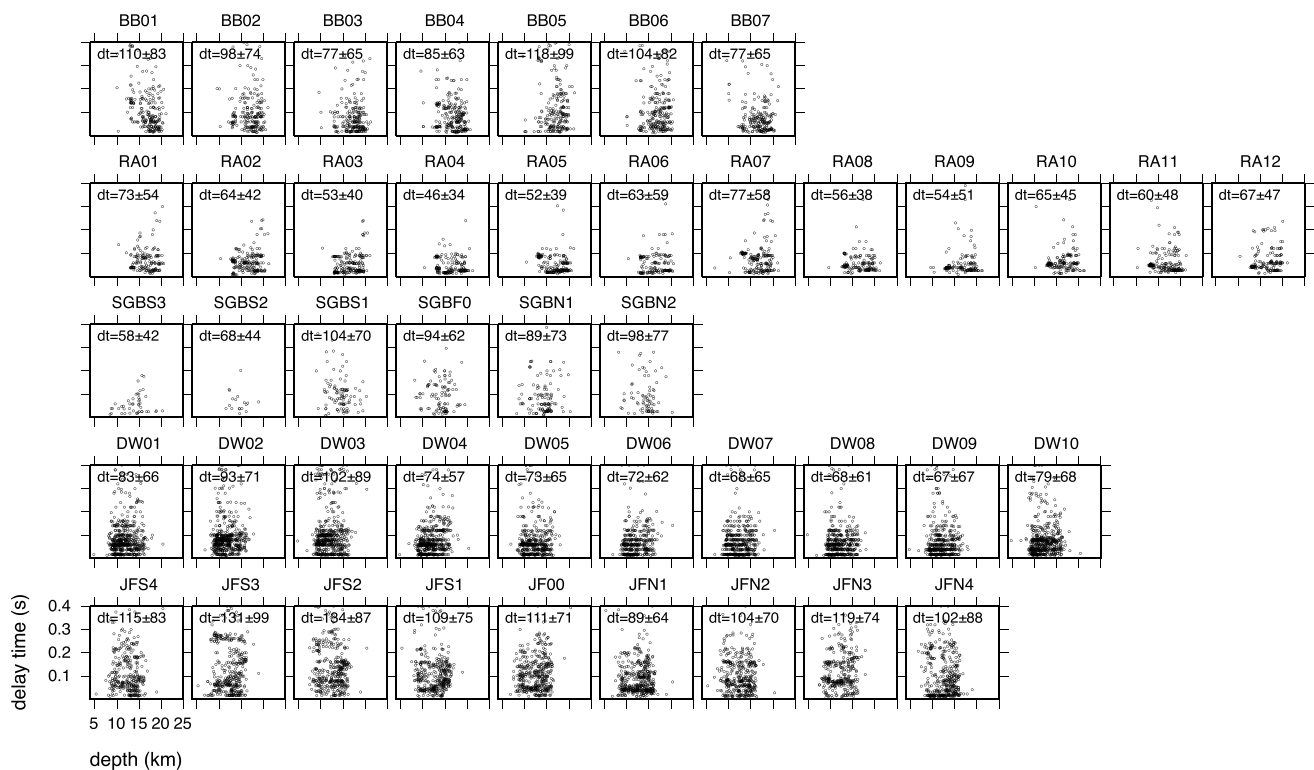


**Figure 5.** Delay times versus event depth on the cross-fault arrays. The station name, average, and standard deviation of  $\delta t$  are marked on top of each panel.

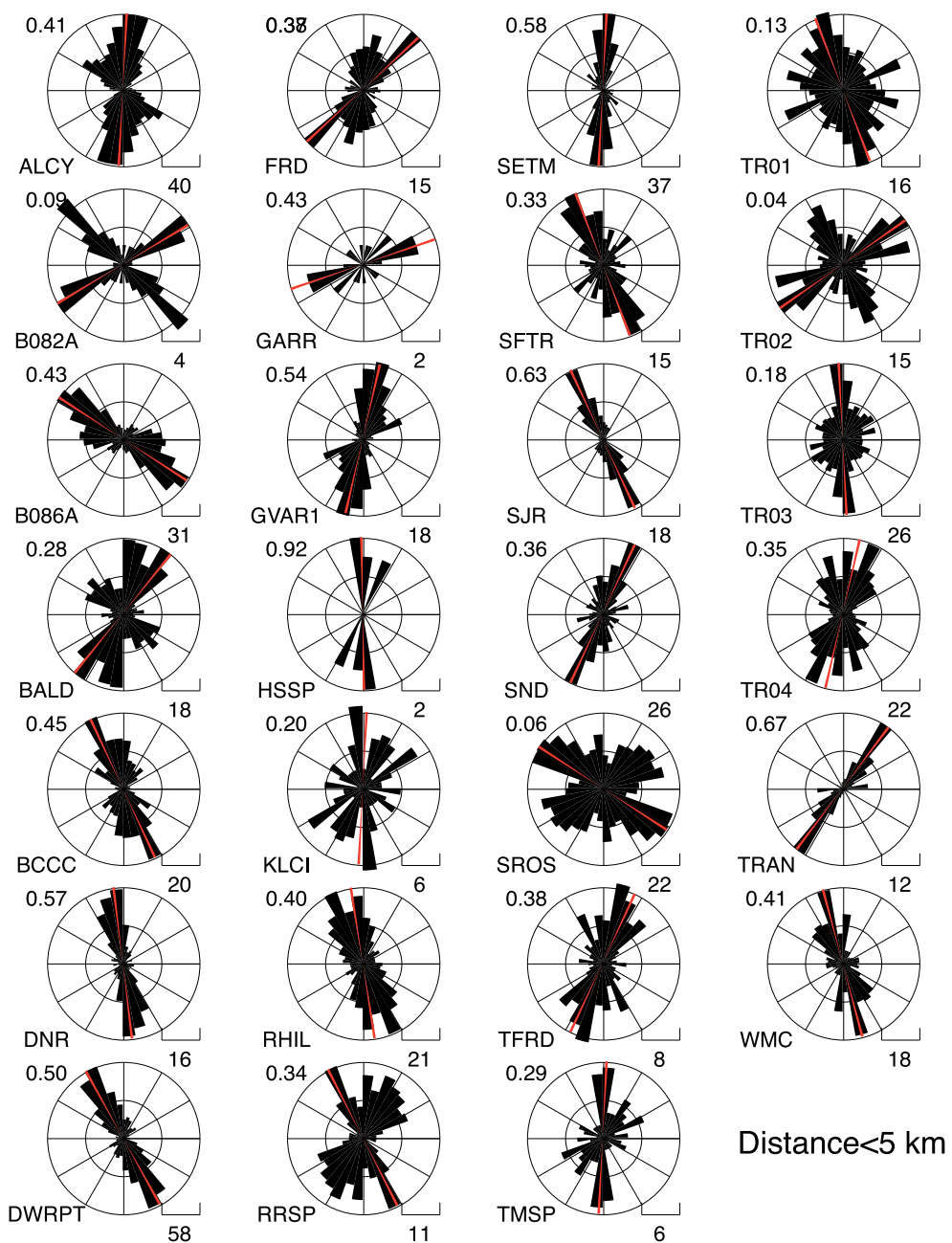


**Figure 6.** Rose diagrams of the fast directions on the stations that are less than 5 km from the main fault. Other symbols/notations are the same as in Figure 4.

#### 4. Results

Average SWS measurements on all arrays and stations are compiled in Tables S1 and S2. Figure 4 shows the rose diagram of fast directions from data of the five linear arrays. The RA array, which is located in the Anza seismic gap, displays highly consistent fast directions. From SW to NE across the fault, the dominant fast directions change gradually from NE-SW to NW-SE. Station RA12, which is at the NE edge of the array and somewhat separated from the remaining stations of the array, shows fast direction along N-S, different from the transition trend shown by stations RA01-RA11. The DW array indicates reasonably consistent fast directions, although with slightly larger scatter, with changing dominant fast directions from NW-SE to NE-SW for stations across the faults (from SW to NE). In contrast to the clear dominant fast directions at the RA and DW

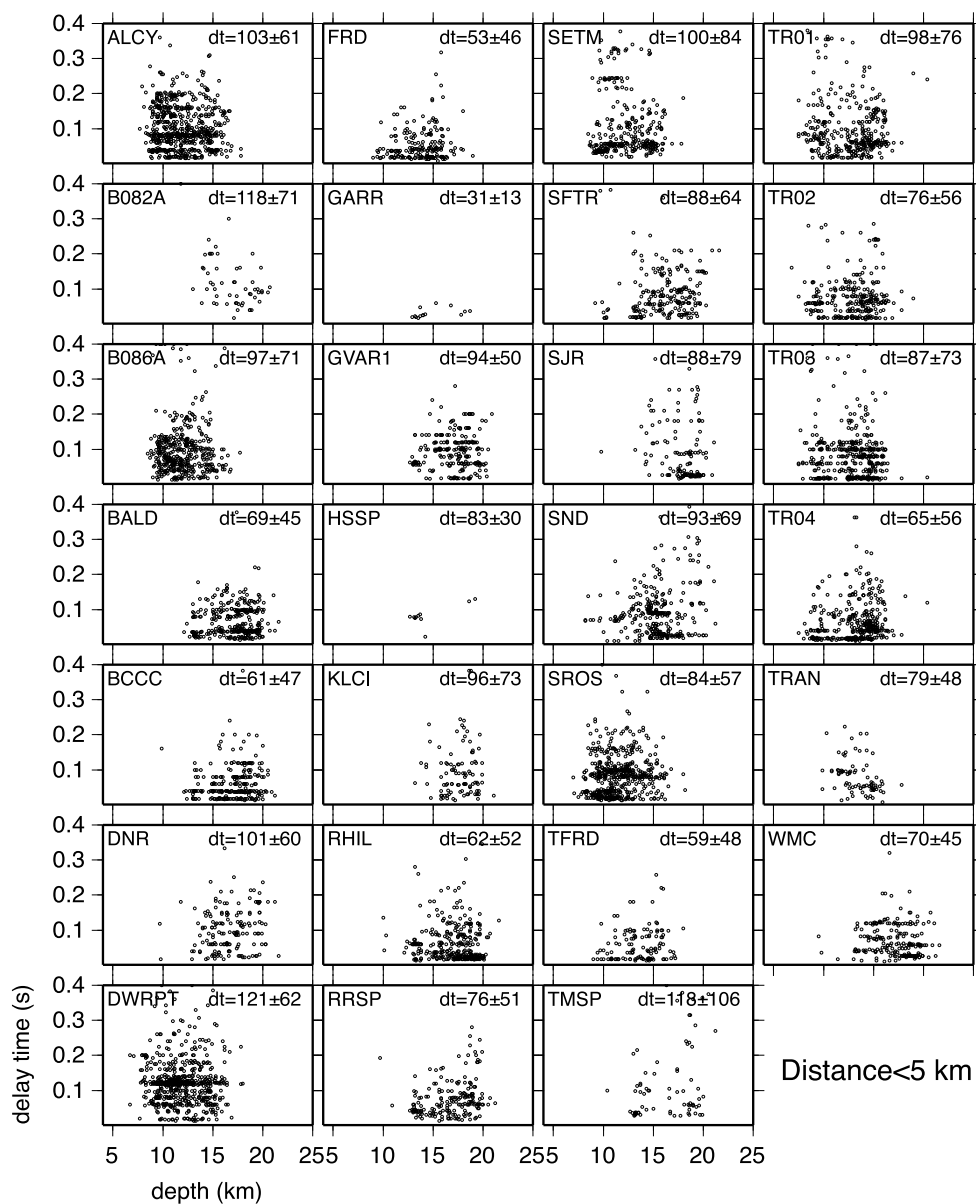


**Figure 7.** Delay times versus event depth on the stations that are 5 km within the main fault. Other symbols/notations are the same as in Figure 5.

arrays, the BB, SGB, and JF arrays show considerable scattering in fast directions. The scattering at the SGB array is partially attributed to the small number of high-quality results (many of the measurements are rejected by the selection criteria.). The BB and JF arrays have many stations with resultant length less than 0.2, showing bimodal or disordered fast directions.

The delay times for all five arrays are plotted against their event depths in Figure 5. Figure S1 provides a similar plot for delay times versus hypocentral distances. The delay times at each station usually have one standard deviation as large as 50–80% of the mean. A general pattern is that the delay times have no significant dependence on event depth at most stations. One possible exception is that at some stations in the RA array the delay times weakly correlate with depths. However, it should be noted that the number of measurements with high delay times on the RA array is smaller than that for the other arrays, making the correlation less reliable.

Figures 6 and 7 display the rose diagrams of fast directions and delay times versus depth for stations that are within 5 km from the main fault branch. Figures 8 and 9 show the same quantities for stations with distance from

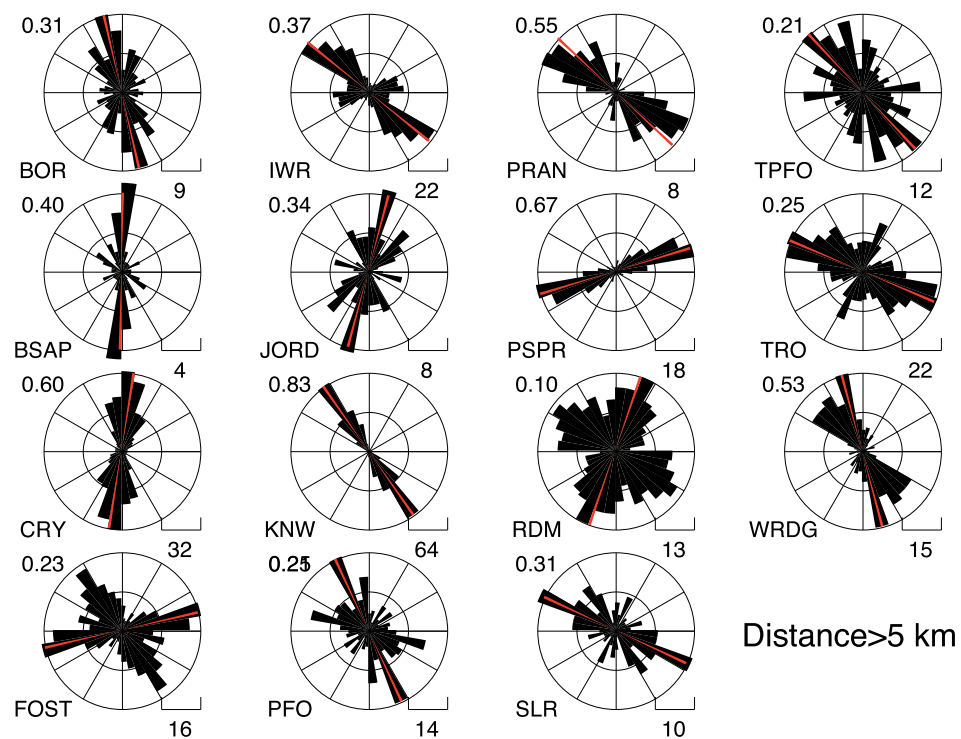


**Figure 8.** Rose diagrams of the fast directions on the stations that are more than 5 km from the main fault. Other symbols/notations are the same as in Figure 4.

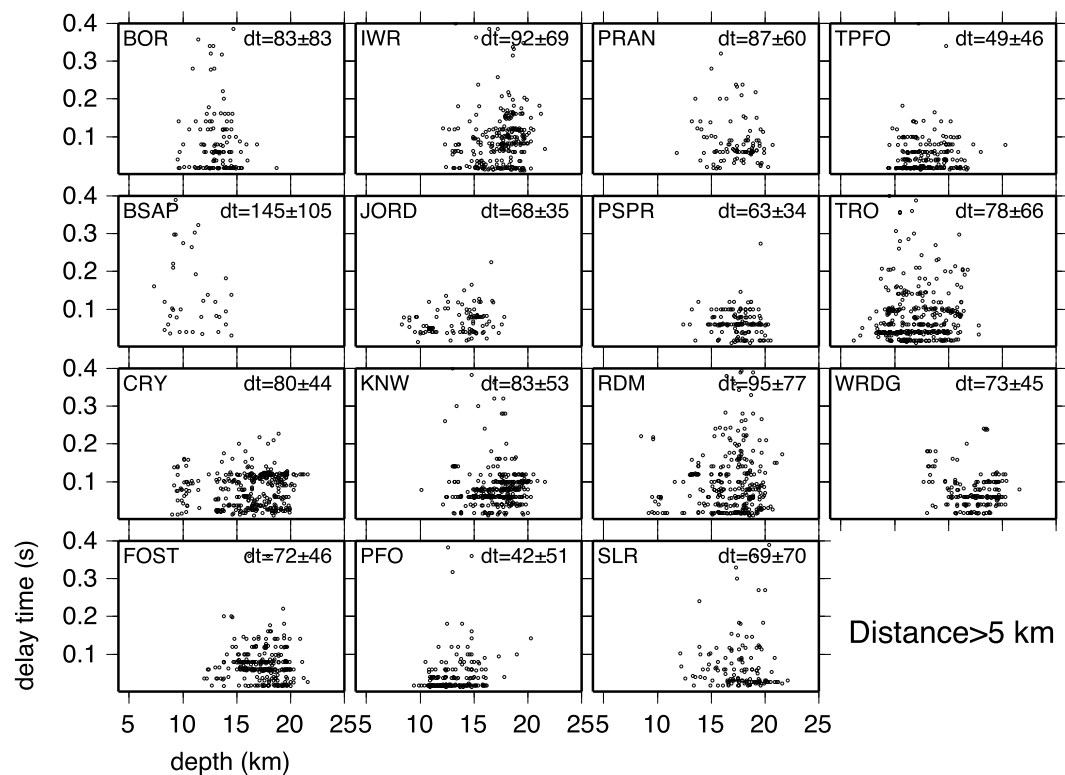


**Figure 9.** Delay times versus event depth on the stations that are more than 5 km from the main fault. Other symbols/notations are the same as in Figure 5.

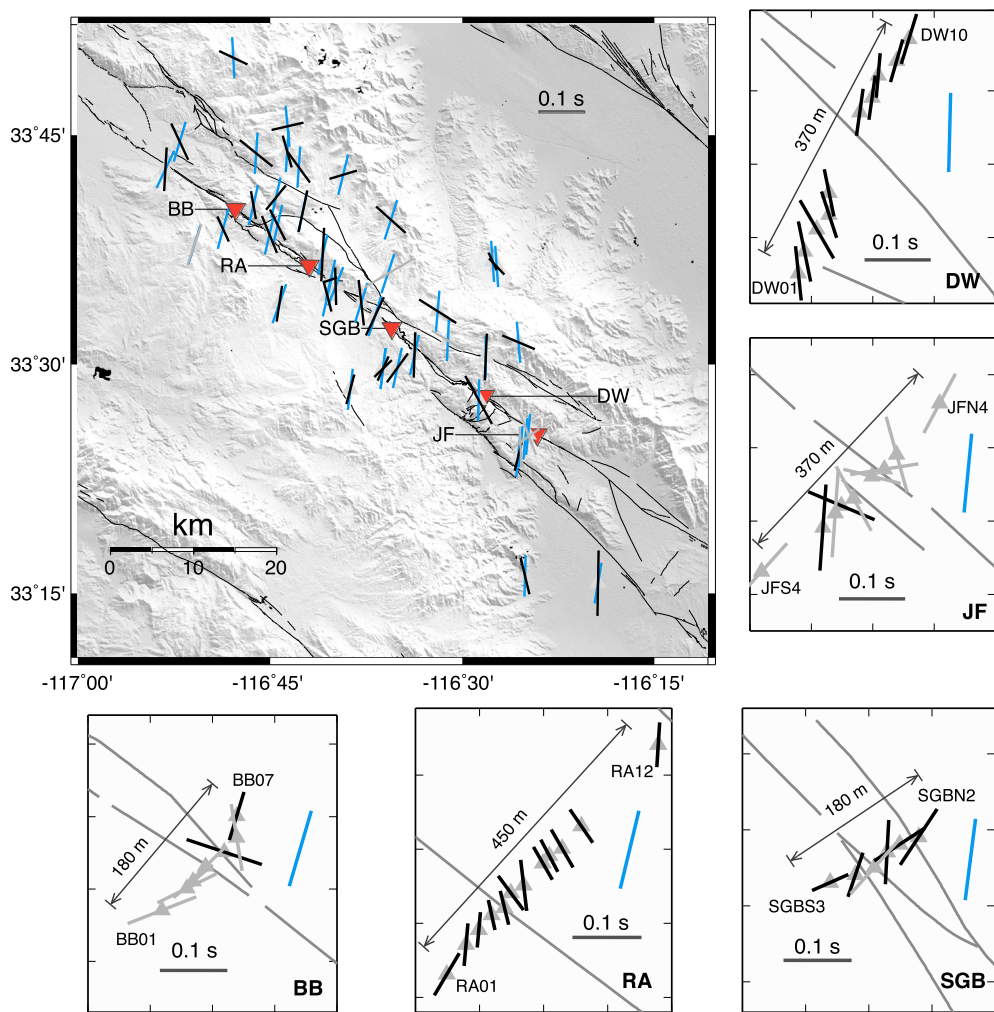


**Figure 10.** Summary of the dominant fast directions and average delay times observed at all stations along the San Jacinto Fault Zone. The gray lines mark the active faults. Black bars are oriented along the dominant fast directions and scaled by the average delay times. Blue bars denote the orientations of maximum horizontal compressive directions from the stress model of Yang and Hauksson [2013]. The five boxes show the zoom-in plots for the five arrays. Gray bars show fast directions with resultant length less than 0.2, indicating poor concentration of fast directions.

the main fault greater than 5 km. The corresponding plots for delay time versus hypocentral distances are shown in Figures S2–S3. We note that this simple grouping criterion cannot be used to judge the distance from individual fault trace, since the SJFZ has complex geometry and multiple branches. Nevertheless, in comparison with the BB, SGB, and JS fault zone arrays, most stations in both groups show clear preferential fast directions (Figures 6 and 8). High scattering in delay times can be seen at individual stations, and there is no significant depth dependence for most stations, except a few such as stations JORD, FRD, RRSP, TMSP, and TFRD (Figures 7 and 9).

Some of the employed stations were included in previous studies, which can be used to check the consistency of results. For example, waveforms recorded at station KNW were analyzed by Peacock *et al.* [1988], Crampin *et al.* [1990], Aster *et al.* [1990], and Yang *et al.* [2011]. All these studies indicated a consistent fast direction about 30° to west, which is also obtained in our analysis (Figure 8). Similar agreement is found for the results associated with stations CRY, DNR, FRD, SND, SRL, and WMC.

Bimodal distributions of fast orientations are observed at some stations, e.g., TR02 and SROS (Figure 6) and FOST and RDM (Figure 8). These may result from multiple mechanisms present in the vicinity of the stations [e.g., Peng and Ben-Zion, 2004]. Analyzing the back azimuthal dependence of SWS measurements can clarify the origin of different mechanisms. To explore this, we project the measurements for each station in

stereonet but find no evidence of back azimuthal dependence at these stations (Figures S4–S6). For example, station FOST has two preferential directions, N40°W and N80°E. The event clusters both from the SW and NW display a mixture of the two patterns. This indicates that there are likely pervasive mixed anisotropy mechanisms (or conjugate joint fractures) surrounding the stations with bimodal distributions.

Figure 10 provides a summary map of the mean fast directions scaled by the mean delay times. The preferential fast directions are plotted with SHmax derived from the focal mechanism inversions of *Yang and Hauksson [2013]*. A general observation is that stations on the SW side of the fault show fast directions largely consistent with the SHmax direction. In contrast, the fast directions on the NE side of the fault show mixed patterns. Some fast directions are subparallel to fault strike (e.g., IWR, PRAN, B086A, and TRO), while others are parallel or subparallel to the SHmax direction (e.g., GVAR1 and BALD), and a few are neither parallel to the fault nor the SHmax direction (e.g., PSPR and FOST).

Stations that are close to the SJFZ (including the across-fault arrays) also indicate mixing patterns. Around the Anza seismic gap (approximately from the RA to SGB array), the fast directions agree well with the SHmax direction at stations TMSP, HSSP, WMC, DNR, and SETM. As mentioned, the RA array in this region shows clear preferential fast directions, with a gradual change across the fault from NE-SW to NW-SE. At the SGB array, the fast directions are rather scattered (Figure 4), but the mean fast directions are generally to the NE-SW, roughly perpendicular to the SJFZ strike. The fast directions at array BB are also scattered, and the dominant directions are to the NE-SW for stations on the SW side and nearly N-S for stations on the NE side. Between arrays BB and RA, the fast directions at stations RHIL, RRSP, and SFTR are aligned between the SJFZ fault strike and the SHmax directions. Close to arrays DW and JF, station SROS has fast direction parallel to the SJFZ fault, while station ALCY has fast direction parallel to the SHmax direction, consistent with the fast directions at the five stations NE of the fault in the DW array. In comparison, station DWRPT immediately to the SW of array DW has a fast direction that is between the SHmax direction and the SJFZ strike, consistent with the directions at the five stations in the DW array SW of the fault. Finally, stations near array JF have fast directions that are either parallel to the SHmax direction or at a high angle to it, consistent with the scattered patterns observed within the JF array (Figure 4).

## 5. Discussion and Conclusions

We systematically measured the SWS parameters within and around the SJFZ, using seismograms recorded by five across-fault linear arrays and various standalone stations (Figure 1). The recording stations sample properties of fault zone damage and the opposite sides of the fault at various sections of the SJFZ. The results are generally compatible with those from previous studies [e.g., *Aster and Shearer, 1992; Yang et al., 2011*], but we also find significant variations of shear wave anisotropy in both along-strike and across-fault directions in the SJFZ.

In general, stations on the SW side of the fault have fast directions that align well with nearly N-S SHmax direction. The stress field derived from focal mechanism inversions shows no distinct variations, and most of SHmax directions have very small angle with respect to the north [*Yang and Hauksson, 2013*]. This suggests that anisotropy on the SW side of the SJFZ is likely controlled by regional maximum compressive stress [e.g., *Yang et al., 2011*]. On the other hand, many stations on the NE sides have fast directions that are subparallel to the local fault strike. A few stations also have fast directions that are almost normal to the SJFZ strike (e.g., GVAR1 and BALD).

The regions around active fault sections within the broad damage zones indicated by tomographic studies [*Allam and Ben-Zion, 2012, 2014; Zigone et al., 2015*] have mixed orientations. Stations in the Anza gap (NW of the trifurcation area) generally have fast directions that are parallel to the regional SHmax directions. However, stations in the trifurcation area (SE of array SGB) have scattered fast directions. While some stations have near-fault parallel directions (e.g., SROS), others have fast directions closer to the SHmax directions (e.g., ALCY and SETM), consistent with the complex fault geometries and damaged rocks in this region. Finally, the fast directions associated with the dense arrays RA and DW show systematic variations across the fault. The measurements at the other three dense arrays are more scattered.

Previous studies suggested that the crustal anisotropy at some stations around the SJFZ were controlled by local alignment of anisotropic layers. For example, *Aster and Shearer [1992]* documented that the well-defined initial shear wave polarization of N40°W at station KNW is consistent with the local alignment of anisotropic

bedrock minerals such as biotite. In the region of station KNW, the NE side of the SJFZ is rather complex with multiple fault branches (e.g., the Hot Spring Fault, the Thomas Mountain Fault, and the Buck Ridge Fault) and several mountains with changing topographies (the San Jacinto and Santa Rosa Mountains) covered by sedimentary and metamorphic rocks. Since sedimentary bedding and mineral alignments in metamorphic rocks can lead to structural-induced anisotropy that is different from stress-induced anisotropy, it is possible that mixed fast directions along and to the NE side of the SJFZ could be produced by anisotropic bedrock layers within a relatively small region.

We do not have detailed local geological information for all stations to confirm whether local rock properties are the primary reason for fast directions not consistent with the regional stress field. Nevertheless, we argue that shear wave anisotropy in various stations around the SJFZ are likely controlled by fault zone rock damage. For example, the fast orientations at array RA in the Anza gap changes systematically from nearly N-S (regional SHmax) directions to subparallel fault direction. This is consistent with the rock damage asymmetry (shifted to the NE) observed from field mapping [Dor *et al.*, 2006], fault zone trapped waves [Lewis *et al.*, 2005], and local earthquake tomography [Allam and Ben-Zion, 2012; Allam *et al.*, 2014]. High angle of polarization to the strike of damage zones may reflect stiffness anisotropy (i.e., low stiffness normal to the damage zone) observed at other active faults [Pisciutta *et al.*, 2012, 2013].

We note that the results have significant variations of fast directions over the short-aperture across-fault arrays, as well as scattered delay times at single stations. Some values could be affected by measurement errors and/or other fault zone-related signals. For example, cycle skipping (i.e., matching between the fast wave and slow wave with a cycle shift) could result in erroneous measurements of both fast directions and delay times. Although the employed MFAST program utilizes a multiple-window approach to mitigate this issue, it may not remove it completely [Savage *et al.*, 2010]. In addition, beyond shear wave splitting, damaged rocks and velocity contrasts in the fault zone structure produce additional seismic phases such as fault zone head waves [Ben-Zion and Aki, 1990; Ben-Zion and Malin, 1991], trapped waves [Ben-Zion and Aki, 1990; Lewis *et al.*, 2005], and diffracted waves [Yang and Zhu, 2010] and various scattered phases [Hong and Menke, 2006; Hillers *et al.*, 2013]. In particular, fault zone head waves and diffracted waves may arrive earlier than the first arrivals and smear the waveform of direct S waves, leading to the erroneous in SWS measurement. For example, Figure 2b shows precursory signals before the large-amplitude S wave at stations RA01–RA04. This is interpreted as the splitting signals, but we cannot rule out the possibility that they are generated by other causes (fault zone refraction/diffraction). These complications may result in scattered measurements observed at some fault zone (and some off-fault) stations.

As mentioned, the fast directions in the Anza gap (starting from the RA array and ending slightly south to the SGB array) agree with the SHmax estimates. The Anza gap is in the central portion of the SJFZ, and it is geometrically simple with an active surface trace connected with the Clark Fault farther to the south. The agreement between the fast directions and SHmax is consistent with this simple geometry. Although scattered, most delay times at array RA are less than 0.1 s (Figure 5), and the mean value is less than those observed at other across-fault arrays (Figure 10). This suggests that the degree of anisotropy is less at array RA, as compared with other arrays. Yang *et al.* [2014] examined P arrival travel time differences across the fine linear fault zone arrays and found relatively small time differences between the two-end stations at array RA, suggesting that low-velocity damage zone is less developed in the Anza gap.

The inclusion in the analysis data from five dense across-fault arrays allows us to study spatial variations of anisotropy in a fault zone region at scales of tens of meters. Arrays JF and BB have scattered fast directions, while array SGB has fast directions that are nearly perpendicular to the local fault strike. Arrays RA and DW have more consistent fast directions, and they also vary systematically across the fault (Figures 4 and 10). In particular, the fast directions at the RA array in the relatively simple Anza section change from nearly stress parallel (SW side) to fault parallel (NE side). The largest change is observed right across the surface fault trace (RA07). At station RA01 and RA12 in both ends of the array, the fast direction returns to be near stress parallel. The pattern is somewhat reversed at array DW in the complex trifurcation area, where the fast directions on the SW side are closer to the fault strike, while those on the NE side of the fault are subparallel to SHmax.

The existence of fractures with nearly fault-parallel direction leads to approximately fault-parallel fast direction, which has been extensively observed in many fault zones [e.g., Savage *et al.*, 1989; Fletcher *et al.*, 1990; Peng and Ben-Zion, 2004; Liu *et al.*, 2005; Boness and Zoback, 2006; Liu *et al.*, 2008]. If we assume that stations in the fault

damage zones record predominately fault-parallel fast directions, our results would imply the existence of damage zones approximately beneath RA06–RA11 for the RA array and beneath DW01–DW05 for the DW array. On the other hand, results from body wave travel times suggest low-velocity zones below RA01–RA07 and DW06–DW12 [Yang *et al.*, 2014], which is almost the opposite from our results. We speculate that these differences are related to the fact that travel time delays (and fault zone trapped waves) are sensitive to the entire crack populations in the low-velocity damage zones, while SWS is mostly controlled by a subset of cracks that has a preferred direction. In this sense, these phenomena are complementary rather than reflecting the same structure. Further analysis is needed to better quantify the location, thickness, and depth extent of the fault damage zone in relation to various seismic signals (e.g., shear wave and stiffness anisotropy and guided waves). This will be the subject of future work.

#### Acknowledgments

This work was supported by the National Science Foundation under grant EAR-0908310 (Z.L. and Z.P.), grant EAR-0908903 (Y.B.Z.), and grant EAR-0908042 (F.L.V.). This research was also supported by the Southern California Earthquake Center (SCEC contribution 6111). SCEC is funded by NSF cooperative agreement EAR-1033462 and USGS cooperative agreement G12AC20038. We thank reviewers Mickaël Bonnin and Martha Savage, Associate Editor Sébastien Chevrot, and Editor Paul Tregoning for their valuable comments. The figures are made from Generic Mapping Tool (GMT). The used seismic waveforms can be obtained from the Data Management Center (DMC) of Incorporated Research Institutions for Seismology (IRIS) at <http://ds.iris.edu/mda/YN?timewindow=2010-2015>.

#### References

- Alford, R. M. (1986), Shear data in presence of azimuthal anisotropy: 56th Ann Internat. Mtg., Soc. Explor. Geophys., Expanded Abstract, 476–479.
- Allam, A. A., and Y. Ben-Zion (2012), Seismic velocity structures in the southern California plate-boundary environment from double-difference tomography, *Geophys. J. Int.*, 190, 1181–1196.
- Allam, A. A., Y. Ben-Zion, I. Kurzon, and F. Vernon (2014), Seismic velocity structure in the hot springs and trifurcation areas of the San Jacinto Fault Zone, California, from double-difference tomography, *Geophys. J. Int.*, 198(2), 978–999, doi:10.1093/gji/ggu176.
- Aster, R. C., and P. M. Shearer (1992), Initial shear wave particle motions and stress constraints at the Anza Seismic Network, *Geophys. J. Int.*, 108, 740–748.
- Aster, R. C., P. M. Shearer, and J. Berger (1990), Quantitative measurements of shear wave polarizations at the Anza seismic network, southern California: Implications for shear wave splitting and earthquake prediction, *J. Geophys. Res.*, 95, 12,449–12,473, doi:10.1029/JB095iB08p12449.
- Audet, P. (2014), Layered crustal anisotropy around the San Andreas Fault near Parkfield, California, *J. Geophys. Res. Solid Earth*, 120, 3527–3543, doi:10.1002/2014JB011821.
- Balfour, N. J., M. K. Savage, and J. Townend (2005), Stress and crustal anisotropy in Marlborough, New Zealand: Evidence for low fault strength and structure-controlled anisotropy, *Geophys. J. Int.*, 163, 1073–1086.
- Ben-Zion, Y., and K. Aki (1990), Seismic radiation from an SH line source in a laterally heterogeneous planar fault zone, *Bull. Seismol. Soc. Am.*, 80, 971–994.
- Ben-Zion, Y., and P. Malin (1991), San-Andreas fault zone head waves near Parkfield, California, *Science*, 251, 1592–1594, doi:10.1126/science.251.5001.1592.
- Boness, N., and M. Zoback (2006), Mapping stress and structurally controlled crustal shear velocity anisotropy in California, *Geology*, 34, 825–828.
- Booth, D. C., and S. Crampin (1985), Shear-wave polarizations on a curved wavefront at an isotropic free-surface, *Geophys. J. R. Astron. Soc.*, 83, 31–45.
- Cochran, E. S., J. E. Vidale, and Y.-G. Li (2003), Near-fault anisotropy following the Hector Mine earthquake, *J. Geophys. Res.*, 108(B9), 2436, doi:10.1029/2002JB002352.
- Cochran, E. S., Y.-G. Li, and J. E. Vidale (2006), Anisotropy in the shallow crust observed around the San Andreas Fault before and after the 2004 M6 Parkfield earthquake, *Bull. Seismol. Soc. Am.*, 96(4B), S364–S375.
- Crampin, S., and Y. Gao (2004), Comment on "Systematic analysis of shear-wave splitting in the aftershock zone of the 1999 Chi-Chi, Taiwan, earthquake: Shallow crustal anisotropy and lack of precursory variations" by Liu, Teng and Ben-Zion, *Bull. Seismol. Soc. Am.*, 95, 354–360.
- Crampin, S., D. Bamford, and R. Mcgonigle (1978), Estimating crack parameters by inversion of P wave velocity anisotropy, *Geophys. J. R. Astron. Soc.*, 53, 173–173.
- Crampin, S., D. C. Booth, R. Evans, S. Peacock, and J. B. Fletcher (1990), Change in shear wave splitting at Anza near the time of the North Palm Springs earthquake, *J. Geophys. Res.*, 95, 11,197–11,212, doi:10.1029/JB095iB07p11197.
- Dor, O., T. K. Rockwell, and Y. Ben-Zion (2006), Geologic observations of damage asymmetry in the structure of the San Jacinto, San Andreas and Punchbowl faults in southern California: A possible indicator for preferred rupture propagation direction, *Pure Appl. Geophys.*, 163, 301–349, doi:10.1007/s00024-005-0023-9.
- Eken, T., M. Bohnhoff, F. Bulut, B. Can, and M. Aktar (2013), Crustal anisotropy in the Eastern Sea of Marmara region in Northwestern Turkey, *Bull. Seismol. Soc. Am.*, 103, 911–924.
- Fialko, Y. (2006), Interseismic strain accumulation and the earthquake potential on the southern San Andreas fault system, *Nature*, 441, 968–971.
- Finzi, Y., E. H. Hearn, Y. Ben-Zion, and V. Lyakhovsky (2009), Structural properties and deformation patterns of evolving strike-slip faults: Numerical simulations incorporating damage rheology, *Pure Appl. Geophys.*, 166, 1537–1573, doi:10.1007/s00024-009-0522-1.
- Fletcher, J. B., T. Fumal, H.-P. Liu, and L. C. Carroll (1990), Near-surface velocities and attenuation at two boreholes near Anza, California, from logging data, *Bull. Seismol. Soc. Am.*, 80, 807–831.
- Gerst, A., and M. Savage (2004), Seismic anisotropy beneath Ruapehu volcano: A possible eruption forecasting tool, *Science*, 306(2004), 1543–1547.
- Godfrey, H. J., A. Shelley, and M. K. Savage (2014), Search for temporal changes in shear-wave splitting associated with the 2012 Te Maari Eruptions at Mount Tongariro, New Zealand, *J. Volcanol. Geotherm. Res.*, 286, 277–93.
- Hamel, Y., V. Lyakhovsky, S. Stanchits, G. Dresen, and Y. Ben-Zion (2009), Brittle deformation and damage-induced seismic wave anisotropy in rocks, *Geophys. J. Int.*, 178, 901–909, doi:10.1111/j.1365-246X.2009.04200.x.
- Hillers, G., Y. Ben-Zion, M. Landès, and M. Campillo (2013), Interaction of microseisms with crustal heterogeneity: A case study from the San Jacinto fault zone area, *Geochem. Geophys. Geosyst.*, 14, 2063–2545, doi:10.1002/ggge.20140.
- Hong, T.-K., and W. Menke (2006), Tomographic investigation of the wear along the San Jacinto fault, southern California, *Phys. Earth Planet. Inter.*, 155, 236–248.
- Kurzon, I., F. L. Vernon, Y. Ben-Zion, and G. Atkinson (2014), Ground motion prediction equations in the San Jacinto Fault Zone—Significant effects of rupture directivity and fault zone amplification, *Pure Appl. Geophys.*, 171, 3045–3081, doi:10.1007/s00024-014-0855-2.

- Leary, P., S. Crampin, and T. McEvilly (1990), Seismic fracture anisotropy in the Earth's crust: An overview, *J. Geophys. Res.*, 95, 11,105–11,114, doi:10.1029/JB095iB07p11105.
- Lewis, M. A., Z. G. Peng, Y. Ben-Zion, and F. L. Vernon (2005), Shallow seismic trapping structure in the San Jacinto Fault Zone near Anza, California, *Geophys. J. Int.*, 162, 867–881.
- Li, Y. G., T. L. Teng, and T. L. Henyey (1994), Shear wave splitting observations in the northern Los Angeles basin, California, *Bull. Seismol. Soc. Am.*, 84, 307–323.
- Li, Z., and Z. Peng (2015), A predict-and-search strategy for picking *P* and *S* phases: Signal-to-noise ratio detector joint with one-dimensional velocity model inversion, *Seismol. Res. Lett.*, 86(2B), 731.
- Li, Z., H. Zhang, and Z. Peng (2014), Structure-controlled seismic anisotropy along the Karadere–Düzce branch of the North Anatolian Fault revealed by shear-wave splitting tomography, *Earth Planet. Sci. Lett.*, 391(2014), 319–326.
- Liu, Y., T. Teng, and Y. Ben-Zion (2004), Systematic analysis of shear-wave splitting in the aftershock zone of the 1999 Chi-Chi, Taiwan, earthquake: Shallow crustal anisotropy and lack of precursory variations, *Bull. Seismol. Soc. Am.*, 94, 2330–2347.
- Liu, Y., Y. Ben-Zion, and T. L. Teng (2005), Reply to comment of Crampin and Gao on "Systematic analysis of shear-wave splitting in the aftershock zone of the 1999 Chi-Chi, Taiwan, earthquake: Shallow crustal anisotropy and lack of precursory variations" by Liu, Teng and Ben-Zion, *Bull. Seismol. Soc. Am.*, 95, 361–366, doi:10.1785/0120040109.
- Liu, Y., H. Zhang, and C. Thurber (2008), Rocker S. Shear wave anisotropy in the crust around the San Andreas fault near Parkfield: Spatial and temporal analysis, *Geophys. J. Int.*, 172, 957–970.
- Magistrale, H., K. McLaughlin, and S. Day (1996), A geology-based 3-D velocity model of the Los Angeles basin sediments, *Bull. Seismol. Soc. Am.*, 86, 1161–1166.
- Mardia, K. V., and P. E. Jupp (2000), *Directional Statistics*, Wiley, Chichester.
- Nur, A., and G. Simmons (1969), Stress-induced velocity anisotropy in rock: An experimental study, *J. Geophys. Res.*, 74(27), 6667–6674, doi:10.1029/JB074i027p06667.
- Peacock, S., S. Crampin, D. C. Booth, and J. B. Fletcher (1988), Shear-wave splitting in the Anza seismic gap southern California: Temporal variations as possible precursors, *J. Geophys. Res.*, 93, 3339–3356, doi:10.1029/JB093iB04p03339.
- Peng, Z., and Y. Ben-Zion (2004), Systematic analysis of crustal anisotropy along the Karadere–Düzce branch of the North Anatolian fault, *Geophys. J. Int.*, 159, 253–274, doi:10.1111/j.1365-246X.2004.02379.x.
- Peng, Z., and Y. Ben-Zion (2005), Spatiotemporal variations of crustal anisotropy from similar events in aftershocks of the 1999 *M*7.4 Izmit and *M*7.1 Düzce, Turkey, earthquake sequences, *Geophys. J. Int.*, 160, 1027–1043, doi:10.1111/j.1365-246X.2005.02569.x.
- Pischutta, M., F. Salvini, J. Fletcher, A. Rovelli, and Y. Ben-Zion (2012), Horizontal polarization of ground motion in the Hayward fault zone at Fremont, California: Dominant fault-high-angle polarization and fault-induced cracks, *Geophys. J. Int.*, 188(3), 1255–1272, doi:10.1111/j.1365-246X.2011.05319.x.
- Pischutta, M., A. Rovelli, F. Salvini, G. Di Giulio, and Y. Ben-Zion (2013), Directional resonance variations across the Pernicana Fault, Mt. Etna, in relation to brittle deformation fields, *Geophys. J. Int.*, 193(2), 986–996, doi:10.1093/gji/ggt031.
- Rasendra, N., M. Bonnin, S. Mazzotti, and C. Tiberi (2014), Crustal and upper mantle anisotropy related to fossilized transpression fabric along the Denali Fault, northern Canadian Cordillera, *Bull. Seismol. Soc. Am.*, 104(4), 1964–1975, doi:10.1785/0120130233.
- Rockwell, T. K., T. E. Dawson, J. Y. Ben-Horin, and G. Seitz (2015), A 21-event, 4000-year history of surface ruptures in the Anza Seismic Gap, San Jacinto Fault, and implications for long-term earthquake production on a major plate boundary fault, *Pure Appl. Geophys.*, 1–23.
- Salisbury, J. B., T. K. Rockwell, T. J. Middleton, and K. W. Hudnut (2012), LiDAR and field observations of slip distribution for the most recent surface ruptures along the central San Jacinto Fault, *Bull. Seismol. Soc. Am.*, 102(2), 598–619.
- Sanders, C. O., and H. Kanamori (1984), A seismotectonic analysis of the Anza Seismic Gap, San Jacinto Fault Zone, southern California, *J. Geophys. Res.*, 89, 5873–5890, doi:10.1029/JB089iB07p05873.
- Savage, M. K., X. R. Shih, R. P. Meyer, and R. C. Aster (1989), Shear-wave anisotropy of active tectonic regions via automated S-wave polarization analysis, *Tectonophysics*, 165, 279–292.
- Savage, M. K., A. Wessel, N. Teanby, and T. Hurst (2010), Automatic measurement of shear wave splitting and applications to time varying anisotropy at Mt. Ruapehu volcano, New Zealand, *J. Geophys. Res.*, 115, B12321, doi:10.1029/2010JB007722.
- Sayers, C. M. (1994), The elastic anisotropy of shales, *J. Geophys. Res.*, 99(B1), 767–774, doi:10.1029/93JB02579.
- Shih, X. R., and R. P. Meyer (1990), Observation of shear wave splitting from nature events: South Moat of Long Valley caldera, California, June 29 to August 12, 1982, *J. Geophys. Res.*, 95, 11,179–11,196, doi:10.1029/JB095iB07p11179.
- Silver, P., and M. Savage (1994), The interpretation of shear-wave splitting parameters in the presence of two anisotropic layers, *Geophys. J. Int.*, 119, 949–963.
- Silver, P., and W. Chan (1991), Shear-wave splitting and subcontinental mantle deformation, *J. Geophys. Res.*, 96, 16,429–16,454, doi:10.1029/91JB00899.
- Sykes, L., and S. Nishenko (1984), Probabilities of occurrence of large plate rupturing earthquakes for the San Andreas, San Jacinto and Imperial faults, California, *J. Geophys. Res.*, 89(B7), 5905–5928, doi:10.1029/JB089iB07p05905.
- Tadokoro K., and M. Ando (2002), Evidence for rapid fault healing derived from temporal changes in *S* wave splitting, *Geophys. Res. Lett.*, 29, 1047, doi:10.1029/2001GL013644.
- Teanby, N., J. Kendall, and M. Van der Baan (2004), Automation of shear-wave splitting measurements using cluster analysis, *Bull. Seismol. Soc. Am.*, 94, 453–463.
- Unglert, K., M. K. Savage, N. Fournier, T. Ohkura, and Y. Abe (2011), Shear wave splitting,  $V_p/V_s$  and GPS during a time of enhanced activity at Aso caldera, Kyushu, *J. Geophys. Res.*, 116, B11203, doi:10.1029/2011JB008520.
- Yang, H., and L. Zhu (2010), Shallow low-velocity zone of the San Jacinto fault from local earthquake waveform modelling, *Geophys. J. Int.*, 183, 421–432.
- Yang, H., Z. Li, Z. Peng, Y. Ben-Zion, and F. L. Vernon (2014), Low-velocity zones along the San Jacinto Fault, Southern California, from body waves recorded in dense linear arrays, *J. Geophys. Res. Solid Earth*, 119, 8976–8990, doi:10.1002/2014JB011548.
- Yang, W., and E. Hauksson (2013), The tectonic crustal stress field and style of faulting along the Pacific North America Plate boundary in Southern California, *Geophys. J. Int.*, 194(1), 100–117, doi:10.1093/gji/ggt113.
- Yang, Z., A. Sheehan, and P. Shearer (2011), Stress-induced upper crustal anisotropy in southern California, *J. Geophys. Res.*, 116, B02302, doi:10.1029/2010JB007655.
- Zhang, Z., and S. Y. Schwartz (1994), Seismic anisotropy in the shallow crust of the Loma Prieta segment of the San Andreas Fault System, *J. Geophys. Res.*, 99(B5), 9651–9661, doi:10.1029/94JB00241.
- Zigone, D., Y. Ben-Zion, M. Campillo, and P. Roux (2015), Seismic tomography of the Southern California plate boundary region from noise-based Rayleigh and Love waves, *Pure Appl. Geophys.*, 172(3), 1007–1032, doi:10.1007/s00024-014-0872-1.